Relativistic random-phase-approximation description of $M1$ excitations with the inclusion of π mesons

Shi Yao Chang (常士尧), Zhi Heng Wang (王之恒), Yi Fei Niu (牛一斐),* and Wen Hui Long (龙文辉)
School of Nuclear Science and Technology, Lanzhou University, Lanzhou 730000, China
and Key Laboratory of Special Function Materials and Structure Design, Ministry of Education, Lanzhou 730000, People's Republic of China

(Received 12 October 2021; accepted 8 March 2022; published 25 March 2022)

Based on the covariant density functional theory, the magnetic dipole ($M1$) resonance is described in the framework of relativistic random-phase approximation with density-dependent meson-nucleon coupling. The isovector-pseudovector interaction channel, represented by the exchange of π meson, is included in the residual interaction to describe unnatural parity transitions. The strength distributions of $M1$ resonances are studied in doubly magic nuclei ^{48}Ca, ^{90}Zr, and ^{208}Pb, in comparison with their analog Gamow-Teller (GT) excitations. It is found that the π meson and its zero-range counterterm are responsible for almost all of the energy shift caused by residual interaction, which is similar to the case of GT excitation. However, the strength of the counterterm suggested by the GT study is not suitable to simultaneously reproduce the experimental $M1$ peak energies from ^{48}Ca to ^{208}Pb. To improve the descriptions of $M1$, effects caused by adjusting the strength of pionic counterterm and introducing the density dependence of the π meson channel are explored. Finally, from the analyses of dominant transition configurations of GT and $M1$ resonance, we find that the proper spin-orbit splitting is the key to simultaneously reproduce the $M1$ strength distributions from light to heavy nuclei.

DOI: 10.1103/PhysRevC.105.034330

I. INTRODUCTION

Magnetic dipole ($M1$) resonance is the lowest-order excitation induced by the electromagnetic field which couples the spin of the nucleon through the nuclear magnetization current [1–3]. The study of $M1$ resonance is of great interest not only for nuclear structure but also for nuclear astrophysics. Since the $M1$ transition is mostly isovector and mostly a spin excitation, it is especially useful for probing the spin-isospin channel of nuclear effective interaction, which is difficult to obtain from ground-state properties of nuclei [1,3]. The spin part of $M1$ operator induces spin-flip transitions between the spin-orbit partners, so it also serves as a good test ground for the description of spin-orbit splitting in nucleus [3]. In astrophysics, the transition strength induced by the isovector spin part of the $M1$ operator determines the cross section of neutral-current inelastic neutrino-nucleus scattering, which is important for supernova simulation [4–7]. Based on the strength distribution of electric dipole ($E1$) and $M1$ excitation, one can obtain the γ-ray strength function (γSF) that determines the neutron capture cross sections [8–10].

In a simple picture, $M1$ transition is composed of two parts [3,11]. One is the orbital magnetic dipole structure, i.e., the scissors mode, which locates in the low-energy region with transition strength proportional to the square of the quadrupole deformation [12,13]. The other part is the spin-flip $M1$ transition in the higher-energy region, and it is mostly determined by single-particle excitation of spin partner states near the Fermi surface. For spherical nuclei, experiments suggest that the scissors motion is strongly suppressed and the spin-flip one is the primary component of $M1$ resonance. In fact, the spin-flip mode is the analog state of the Gamow-Teller (GT) state in the parent nucleus, which provides the spin-orbit splitting information and determines the cross section of inelastic neutrino-nucleus scattering, as mentioned above. In this work, we will focus on the study of $M1$ excitation in doubly magic spherical nuclei.

Experimentally the $M1$ excitation can be realized using electromagnetic and hadronic probes, such as (γ, γ'), (e, e'), and (p, p') reactions [3,11,14–16]. After decades of exploration, large amounts of data have been accumulated [17], which serves a good test ground for nuclear structure models. On the other hand, the benchmarked nuclear models can also be used for predictions of $M1$ transitions, especially for those nuclei far from stability line, which are useful for astrophysical applications, such as neutron capture rates in r-process nucleosynthesis [18,19] or inelastic neutrino scattering in core-collapse supernova [4–7].

There are mainly two kinds of microscopic theoretical model for the study of $M1$ excitation, i.e., the shell model and random-phase approximation (RPA) model. Usually large-scale shell-model calculation is only used for the description of low-energy 0-$\hbar\omega$ $M1$ excitation of light and middle mass nuclei [20,21]. Until recently it is extended to nuclei with mass number $A > 100$ [22]. Compared to the large numerical efforts taken by shell-model calculation, the RPA model provides a much simpler way for the study of $M1$ excitation. In the nonrelativistic framework, self-consistent RPA model based on Skyrme or Gogny density functional has been

*niuyf@lzu.edu.cn

realized. Based on the Skyrme density functional, the spin-flip $M1$ giant resonances were described by the self-consistent RPA model [23–28]. However, there is no published Skyrme parametrization which can simultaneously describe well the $M1$ excitation in ^{208}Pb and other nuclei [25,27–29]. Even with the inclusion of correlations beyond the RPA model, the self-consistent RPA + renormalized time-blocking approximation (RenTBA) based on the Skyrme density functional cannot improve much on the basic experimental characteristics of the $M1$ excitations in ^{208}Pb but can reproduce the observed fragmentation, which is missing in RPA calculations, to a certain extent by some certain Skyrme functionals [30]. Based on the situation that present parametrizations of the Skyrme interaction are not suitable for the description of $M1$ excitations, this calls for a better modeling of spin-orbit term and spin-spin interaction [28]. Aiming for this, the spin-related parameters were modified, and as a result, the energies of the low-lying $M1$ state and the resonance state in ^{208}Pb were both well described [27]. The tensor force is also shown to have a large effect on $M1$ excitations with the Skyrme RPA framework [31,32], and so do the spin-density-dependent terms in the extended Skyrme force [26]. Based on the Gogny density functional, the axially symmetric deformed quasiparticle RPA (QRPA) model was used to describe the $M1$ mode of 412 even-even nuclei. With a shift of excitation energies by 0.5–2 MeV, a relatively good agreement with experimental data was obtained [9]. The role of tensor force and continuum effect were also investigated by the RPA model using Gogny force [33]. It can be seen that within the nonrelativistic framework, it is difficult to well describe the $M1$ excitations using fully self-consistent (Q)RPA models.

In the covariant density functional theory (CDFT), Lorentz invariance allows us to describe the spin-orbit coupling in a self-consistent way, and this symmetry puts stringent restrictions on the number of parameters in the corresponding functionals without reducing the quality of agreement with experimental data [34–40]. Based on the spirit of CDFT, the nucleus is described as a system of Dirac nucleons that interact with each other via the exchange of mesons with the proper relativistic quantum numbers. It provides an efficient and predictive tool to explore the structure properties of nuclei over almost the whole nuclear chart. Varieties of nuclear phenomena have been successfully described: ground-state properties such as binding energies, nuclear charge radii from spherical nuclei to deformed ones [41–50], the origin of the pseudospin symmetry in nucleon single-particle spectrum [51,52], halo phenomena of nuclei observed near the neutron-drip line [39], the magnetic [53] and antimagnetic [54] rotations in nearly spherical nuclei, and the chiral rotation in triaxial nuclei [55–57].

For a description of nuclear vibrations, based on CDFT the proton-neutron relativistic random-phase approximation (pnRRPA) [58–62] and proton-neutron relativistic quasiparticle RPA (pnRQRPA) [63–65] were developed, which have been successfully applied to the description of spin-isospin excitations, so do the relativistic random-phase approximation (RRPA) and relativistic quasiparticle RPA (RQRPA) for giant resonances [66,67]. However, the existing R(Q)RPA model for giant resonances only includes the exchanges of σ, ω, and ρ mesons in the two-body residual interaction. Because of the parity conservation, π meson has no contribution in ground-state calculations within the relativistic mean-field (RMF) model, but it does contribute to the particle-hole (p-h) residual interaction. It has been shown that in the description of GT resonances, π meson and its counterterm included in the residual interaction play essential roles in determining the centroid energy of the resonance [61,63], i.e., being responsible for almost all the energy shift caused by the residual interaction. As the analog state of GT excitations, the correct description of $M1$ excitations necessitates the inclusion of π meson and its counterterm in the residual interaction, just like the pnRQRPA case for charge-exchange excitations. Therefore, the description of giant resonances has been limited to electric transitions for a long time, because additional nuclear interaction channels such as the isovector-pseudovector channel contributed by the π meson required for magnetic transitions are missing in the existing (Q)RPA for giant resonances.

Until recently, RQRPA for the description of $M1$ transitions [68–72] has been realized based on the CDFT with density-dependent point-coupling interactions, which are the simplified zero-range interactions of the finite-range meson-exchange forces. In order to describe the unnatural-parity $M1$ excitations, the isovector-pseudovector interaction channel is included in the residual interactions. The newly introduced parameter for this interaction channel was determined by minimizing the gaps between the theoretically calculated centroid energy and experimentally determined dominant peak position of measured $M1$ transition strength in ^{208}Pb and ^{48}Ca [70]. However, the energies of light systems, e.g., ^{48}Ca, still have some deviations from the experimental data [70]. The pairing correlations show a significant impact on the major peak of $M1$ response functions in open-shell nuclei and its role is mainly observed at the level of the ground-state calculation [68–70].

In this work, based on the density-dependent meson-exchange interactions, we are going to develop the RRPA model by including the π meson and its counterterm in the residual interaction in order to describe the unnatural-parity $M1$ excitations. The $M1$ excitations of doubly magic nuclei ^{48}Ca, ^{90}Zr, and ^{208}Pb will be studied, and compared with their analog GT excitations. The effects of π meson will be investigated in detail, which would reflect important aspects of nuclear force and provide guidance for further development of nuclear effective interaction.

This paper is organized as follows. In Sec. II, we briefly introduce the theoretical framework of the relativistic random-phase approximation. Special attentions are paid to the inclusion of the new interaction channels contributed by π meson and its counterterm. Section III presents results and analysis of model calculations. A summary of the present work is given in Sec. IV.

II. THEORETICAL FRAMEWORK

In the RMF theory, nucleons interact with each other through the exchange of mesons and photons based on the one-boson exchange diagram [34,73,74]. The standard form

of RMF theory is constructed with nucleon field ψ, isoscalar meson fields σ and ω, isovector meson field ρ, and photon field A, with the effective Lagrangian density

$$\begin{aligned}\mathscr{L} &= \bar{\psi}(i\gamma^\mu\partial_\mu - M)\psi - \bar{\psi}\Big(g_\sigma\sigma + g_\omega\gamma^\mu\omega_\mu \\ &+ g_\rho\gamma^\mu\vec{\rho}_\mu\cdot\vec{\tau} + e\gamma^\mu\frac{1-\tau_3}{2}A_\mu\Big)\psi + \frac{1}{2}\partial^\mu\sigma\partial_\mu\sigma \\ &-\frac{1}{2}m_\sigma^2\sigma^2 - \frac{1}{4}\Omega_{\mu\nu}\Omega^{\mu\nu} + \frac{1}{2}m_\omega^2\omega_\mu\omega^\mu \\ &-\frac{1}{4}\vec{R}_{\mu\nu}\cdot\vec{R}^{\mu\nu} + \frac{1}{2}m_\rho^2\vec{\rho}^\mu\cdot\vec{\rho}_\mu - \frac{1}{4}F^{\mu\nu}F_{\mu\nu}, \end{aligned} \tag{1}$$

where M is the bare nucleon mass and m_i ($i = \sigma, \omega, \rho$) are meson masses. The field tensors are defined as

$$\Omega^{\mu\nu} \equiv \partial^\mu\omega^\nu - \partial^\nu\omega^\mu, \tag{2a}$$

$$\vec{R}^{\mu\nu} \equiv \partial^\mu\vec{\rho}^\nu - \partial^\nu\vec{\rho}^\mu, \tag{2b}$$

$$F^{\mu\nu} \equiv \partial^\mu A^\nu - \partial^\nu A^\mu. \tag{2c}$$

From the effective Lagrangian Eq. (1), we can derive the Hamiltonian $\hat{H}$ through the Legendre transformation, which reads

$$\begin{aligned}\hat{H} &= \int d^3x_1\bar{\psi}(-i\boldsymbol{\gamma}\cdot\boldsymbol{\nabla} + M)\psi + \frac{1}{2}\iint d^3x_1d^4x_2 \\ &\times\sum_{i=\sigma,\omega,\rho,A}\bar{\psi}(x_1)\bar{\psi}(x_2)\Gamma_i(1,2)D_i(1,2)\psi(x_2)\psi(x_1),\end{aligned} \tag{3}$$

where $\Gamma_i(1,2)$ are the interaction vertices

$$\Gamma_\sigma(1,2) = -g_\sigma(1)g_\sigma(2), \tag{4a}$$

$$\Gamma_\omega(1,2) = +g_\omega(1)\gamma_\mu(1)g_\omega(2)\gamma^\mu(2), \tag{4b}$$

$$\Gamma_\rho(1,2) = +g_\rho(1)\gamma_\mu(1)\vec{\tau}(1)\cdot g_\rho(2)\gamma^\mu(2)\vec{\tau}(2), \tag{4c}$$

$$\Gamma_A(1,2) = +\frac{e^2}{4}[\gamma_\mu(1-\tau_3)]_1[\gamma^\mu(1-\tau_3)]_2. \tag{4d}$$

The propagators $D_i(1,2)$ in the Hamiltonian are

$$D_i(1,2) = -\int\frac{d^4k}{(2\pi)^4}e^{-ik(x_1-x_2)}\frac{1}{k^2-m_i^2}. \tag{5}$$

Taking a Slater determinant $|\Phi_0\rangle$ as the trial ground state, the energy functional can be expressed as

$$\begin{aligned}E &= \langle\Phi_0|\hat{H}|\Phi_0\rangle = \langle\Phi_0|\hat{T}|\Phi_0\rangle + \langle\Phi_0|\hat{V}|\Phi_0\rangle \\ &= \sum_i\langle i|-i\boldsymbol{\alpha}\cdot\boldsymbol{\nabla} + \beta M|i\rangle + \frac{1}{2}\sum_{ij}\langle ij|V(1,2)|ij\rangle,\end{aligned} \tag{6}$$

where the sum over i and j runs over all the occupied single-particle states in the Fermi sea. Note that the Fock term is neglected in the Hartree approximation, and its contribution will be taken into account through the parametrization of the effective interactions. The variation of the energy E with respect to the single-particle state leads to the single-particle Dirac equation, which can be solved iteratively. More details are in Refs. [40,75] as well as the references therein.

The density-dependent form of effective interaction is adopted in this work [76], i.e., the meson-nucleon coupling constants are treated as a function of baryonic density ρ_b. For σ and ω channel, it is defined as follows:

$$g_i(\rho_b) = g_i(\rho_0)f_i(\xi), \qquad \text{for} \qquad i = \sigma, \omega, \tag{7}$$

where

$$f_i(\xi) = a_i\frac{1+b_i(\xi+d_i)^2}{1+c_i(\xi+d_i)^2} \tag{8}$$

is a function of $\xi = \rho_b/\rho_0$ and ρ_0 is the saturation density in symmetric nuclear matter. For isovector meson ρ channel, the ρ-N coupling constants reads

$$g_\rho(\rho_b) = g_\rho(\rho_0)e^{-a_\rho(\xi-1)}. \tag{9}$$

Note that $g_i(\rho_0)$, $g_\rho(\rho_0)$, a_ρ, a_i, b_i, c_i, and d_i are parameters of the density-dependent effective interaction [77].

Now let us consider a system under a time-dependent external field $F(t) = Fe^{-i\omega t} + F^\dagger e^{i\omega t}$. In this case, the wave function of the system, $\Phi(t)$, is no longer a static one. The density operator ρ satisfies the following equation of motion:

$$i\dot{\rho} = [h[\rho] + F(t), \rho]. \tag{10}$$

The $h[\rho]$ in Eq. (10) is the single-particle Hamiltonian. With the small-amplitude limit, the RPA equation can be derived as

$$\begin{pmatrix} A^J & B^J \\ -B^{J*} & -A^{J*}\end{pmatrix}\begin{pmatrix} X^{\nu JM} \\ Y^{\nu JM}\end{pmatrix} = E^\nu\begin{pmatrix} X^{\nu JM} \\ Y^{\nu JM}\end{pmatrix}, \tag{11}$$

where the matrix elements of A and B are defined as

$$\begin{aligned}A^J &= \begin{bmatrix}(\epsilon_p-\epsilon_h)\delta_{pp'}\delta_{hh'} & 0 \\ 0 & (\epsilon_\alpha-\epsilon_h)\delta_{\alpha\alpha'}\delta_{hh'}\end{bmatrix} \\ &+\begin{pmatrix}V^J_{ph'hp'} & V^J_{ph'h\alpha'} \\ V^J_{\alpha h'hp'} & V^J_{\alpha h'h\alpha'}\end{pmatrix},\end{aligned} \tag{12}$$

$$B^J = \begin{bmatrix}(-1)^{j_{h'}-j_{p'}+J}V^J_{pp'hh'} & (-1)^{j_{h'}-j_{\alpha'}+J}V^J_{p\alpha'hh'} \\ (-1)^{j_{h'}-j_{p'}+J}V^J_{\alpha p'hh'} & (-1)^{j_{h'}-j_{\alpha'}+J}V^J_{\alpha\alpha'hh'}\end{bmatrix}. \tag{13}$$

In the relativistic case with no-sea approximation, antiparticle-hole configurations denoted by α-h are also included in building the RRPA matrix [60]. Hereafter, we use p-h to denote the configuration constructed by the unoccupied and occupied states in the Fermi sea. Note that in Eq. (11) we directly present the angular-momentum coupled form of the RPA equation, which is convenient for the nuclei with spherical symmetry; see more details in Ref. [66]. The V^J are angular-momentum coupled two-body interaction matrix elements in p-h or α-h channel, which are defined as

$$\begin{aligned}V^J_{abcd} &= \sum_{m_am_cm_dm_b}C^{JM}_{j_am_aj_c-m_c}C^{JM}_{j_dm_dj_b-m_b} \\ &\times(-1)^{j_c-m_c+j_b-m_b}V_{abcd}.\end{aligned} \tag{14}$$

We can obtain the eigenvalue E^ν and corresponding amplitudes $X^{\nu JM}$ and $Y^{\nu JM}$ of collective state $|\nu_{JM}\rangle$ with the angular momentum JM by diagonalizing the RPA matrix in Eq. (11). Finally, the transition strength B^{JM}_ν from the ground state $|0\rangle$

to the excited state $|\nu_{JM}\rangle$ induced by the operator $\hat{W}_{JM}$ reads

$$B_\nu^{JM} = \Big| \hat{J}^{-1} \sum_{cd} \big(X_{cd}^{\nu JM} \langle c||W_{JM}||d\rangle + (-1)^{j_d - j_c + J} Y_{cd}^{\nu JM} \langle d||W_{JM}||c\rangle \big) \Big|^2, \quad (15)$$

where both the p-h and α-h configurations are considered.

To obtain a smooth strength distribution, the discrete transition strength B_ν^{JM} is usually folded through a Lorentzian function, and the response function $R(E)$ thus reads

$$R(E) = \sum_\nu B_\nu \frac{\Gamma/2\pi}{(E - E^\nu)^2 + \Gamma^2/4}, \quad (16)$$

where the width Γ is taken to be 1 MeV in this work.

It is well known that the degree of freedom of π meson makes no contribution to the ground state under the Hartree approximation because of the parity conservation. While for the description of excitations in the relativistic random-phase approximation, the isovector-pseudovector interaction channel contributed by exchanging π meson should be involved in the residual interaction. The Lagrangian $\mathcal{L}_\pi$ related to the π-N coupling reads

$$\mathcal{L}_\pi = -\frac{f_\pi}{m_\pi} \bar{\psi} \gamma_5 \gamma^\mu \partial_\mu \vec{\pi} \vec{\tau} \psi. \quad (17)$$

In addition, to cancel the contact term of the π-N coupling, a Landau-Migdal zero-range counterterm is included [63,78,79], which reads

$$V^{\delta\pi}(1,2) = g' \left(\frac{f_\pi}{m_\pi} \right)^2 \vec{\tau}_1 \cdot \vec{\tau}_2 [\gamma_5 \boldsymbol{\alpha}]_1 \cdot [\gamma_5 \boldsymbol{\alpha}]_2 \delta(\boldsymbol{r}_1 - \boldsymbol{r}_2). \quad (18)$$

The parameter g' in the zero-range counterterm is an adjustable parameter with the value $g' \approx 0.6$ [63,79] to reproduce experimental data of GT excitation in pnRRPA approach. For the RMF effective interactions DD-ME2 [77], DD-ME1 [80], and PKDD [81], the values of g' are taken as 0.52, 0.55, and 0.56, respectively. In this work, we mainly use the effective interaction DD-ME2. The value of g' is first taken as 0.52, which is the same as that for the GT calculation. Then the optimal values for $M1$ excitations for three interactions DD-ME2, DD-ME1, and PKDD will be discussed in Sec. III. Usually, the pion mass and coupling constant are taken as [63]

$$m_\pi = 138 \text{ MeV}, \qquad \frac{f_\pi^2}{4\pi} = 0.08. \quad (19)$$

For the $M1$ transition ($J^\pi = 1^+$) induced by external magnetic field, the form of transition operator $\hat{W}(M1)$ is expressed as

$$\hat{W}(M1) = \sqrt{\frac{3}{4\pi}} \sum_i [g_l(i) \boldsymbol{l}_i + g_s(i) \boldsymbol{s}_i] \mu_N, \quad (20)$$

where $\mu_N = e\hbar/2m_N$ is the nuclear magneton with m_N being nucleon mass; $\boldsymbol{l}_i$ and $\boldsymbol{s}_i$ are the orbital and spin angular momenta, respectively; and $g_l(i)$ and $g_s(i)$ are the corresponding g factors of nucleons. The values of the g factor for neutron (ν) and proton (π) are

$$g_s^\nu = -3.826, \quad g_l^\nu = 0$$
$$g_s^\pi = 5.586, \quad g_l^\pi = 1, \quad (21)$$

where the g factors for free protons and neutrons are used [16,82].

In analogy to the electric excitation operator, the $M1$ operator can be separated into isoscalar (IS) and isovector (IV) components by using the expressions for the g factor in terms of isospin [16]. With the third component of isospin $\tau_3(i) = \pm 1$ for neutrons and protons, respectively, the $M1$ operator can be rewritten as the sum of IS and IV terms:

$$\hat{W}(M1) = \sqrt{\frac{3}{4\pi}} \sum_i \big(g_l^{\rm IS} \boldsymbol{l}_i + g_s^{\rm IS} \boldsymbol{s}_i \big) \mu_N + \sqrt{\frac{3}{4\pi}} \sum_i \big(g_l^{\rm IV} \boldsymbol{l}_i + g_s^{\rm IV} \boldsymbol{s}_i \big) \tau_3(i) \mu_N. \quad (22)$$

The IS and IV combinations of g factors are

$$g_l^{\rm IS} = \frac{g_l^\pi + g_l^\nu}{2} = 1/2, \quad (23)$$

$$g_l^{\rm IV} = \frac{g_l^\nu - g_l^\pi}{2} = -1/2, \quad (24)$$

$$g_s^{\rm IS} = \frac{g_s^\pi + g_s^\nu}{2} = 0.880, \quad (25)$$

$$g_s^{\rm IV} = \frac{g_s^\nu - g_s^\pi}{2} = -4.706. \quad (26)$$

Since $g_s^{\rm IV}$ is much larger than $g_s^{\rm IS}$, the $M1$ operator is dominantly isovector in nature.

Up to now, there has not existed appropriate sum rule of $M1$ excitation which is derived from RMF theory. The well-known Kurath sum rule [83] is one of the available criteria that we can adopt. It should be noted that the original Kurath sum rule only refers to the IV components of the $M1$ excitation, which reads [83,84]

$$m_1(M1) \cong \frac{3\mu_N^2}{4\pi} \big(g_s^{\rm IV} - g_l^{\rm IV} \big)^2 \sum_i (-a_{\rm so}) \langle \boldsymbol{l}(i) \cdot \boldsymbol{s}(i) \rangle. \quad (27)$$

In Eq. (27), the coefficient $a_{\rm so}$ indicates the strength of non-relativistic spin-orbit coupling interaction utilized by Kurath [83], and the bracket means the expectation value for the ground state. In this work, the $M1$ operator used for the calculation of $M1$ excitation strength, i.e., Eq. (22), consists of both the IV and the IS components, so the Kurath sum rule is expressed as

$$m_1(M1) = \frac{3}{4\pi} \mu_N^2 \big[\big(g_s^{\rm IS} - g_l^{\rm IS} \big)^2 + \big(g_s^{\rm IV} - g_l^{\rm IV} \big)^2 \big] \sum_i \langle [-a_{{\rm so},i}(r)] \boldsymbol{l}_i \cdot \boldsymbol{s}_i \rangle + \frac{3}{2\pi} \mu_N^2 \big(g_s^{\rm IV} - g_l^{\rm IV} \big) \big(g_s^{\rm IS} - g_l^{\rm IS} \big) \sum_i \langle [-a_{{\rm so},i}(r)] \boldsymbol{l}_i \cdot \boldsymbol{s}_i \tau_3(i) \rangle, \quad (28)$$

where the interference term between IV and IS components also appears in the Kurath sum rule.

Since the Hamiltonian in the RMF theory does not display the spin-orbit coupling term explicitly, there is not a parameter corresponding to $a_{\rm so}$. In order to get the spin-orbit coupling strength in RMF theory, a Schrödinger-like equation [35,36] for the large components of Dirac spinors $G(r)$ is deduced, which reads

$$\left\{\vec{p}\frac{1}{2M_{\rm eff}(r)}\vec{p}+[V(r)+S(r)]+V_{\rm so}(r)\right\}G_i(r)=\epsilon_i G_i(r). \tag{29}$$

In Eq. (29), the spin-orbit term can be expressed as

$$V_{\rm so}(r)=\frac{1}{2M_{\rm eff}^2(r)}\frac{1}{r}\frac{d}{dr}[V(r)-S(r)]\boldsymbol{l}\cdot\boldsymbol{s}, \tag{30}$$

where the effective mass $M_{\rm eff}$ reads

$$M_{\rm eff}(r)=M-\tfrac{1}{2}[V(r)-S(r)]. \tag{31}$$

So the spin-orbit coupling strength $a_{{\rm so},i}(r)$ in RMF theory is

$$a_{{\rm so},i}(r)=\frac{1}{2M_{\rm eff}^2}\frac{1}{r}\frac{d}{dr}[V(r)-S(r)], \tag{32}$$

which is a function of coordinate r and depends on the single-particle states. By calculating the expectation value in Eq. (28), we can get the corresponding $a_{\rm so,i}$ in RMF theory, which reads

$$a_{{\rm so},i}=\int dr G_i^2(r)\frac{1}{2M_{\rm eff}^2}\frac{1}{r}\frac{d}{dr}[V(r)-S(r)]. \tag{33}$$

III. RESULTS AND DISCUSSIONS

In this section, based on the RMF + RPA approach including the π meson, we shall study the $M1$ transition strength distributions in three magic nuclei ^{48}Ca, ^{90}Zr, and ^{208}Pb. Density-dependent effective interactions DD-ME2, DD-ME1, and PKDD are employed in the calculations. To explore the residual interaction of π-PV coupling in nuclear medium, the corresponding results by introducing a density-dependent form of coupling constant f_π are also presented.

In Fig. 1, we show the strength distributions of the $M1$ excitations in ^{48}Ca, ^{90}Zr, and ^{208}Pb, calculated by RMF+RPA using interaction DD-ME2. For comparison, the strength distributions of their analog excitations, i.e., GT excitations, calculated by RMF+pnRPA are also shown. In order to investigate the contributions of different interaction channels, especially the isovector-pseudovector π-N coupling channel, the results of unperturbed calculation and those calculations by adding successively the residual interaction from different meson-nucleon couplings on top of it are also presented in Fig. 1. For $M1$ excitation, the ω-, ρ-, and π-meson fields and photon field contribute to the residual interaction in RRPA calculations, while for GT excitation, only ρ- and π-meson fields of isovector nature contribute. Here the parameter g' in the zero-range counterterm for GT and $M1$ calculations is taken as 0.52 for both cases, which is a standard value in pnRRPA calculations for interaction DD-ME2, suggested in Ref. [63].

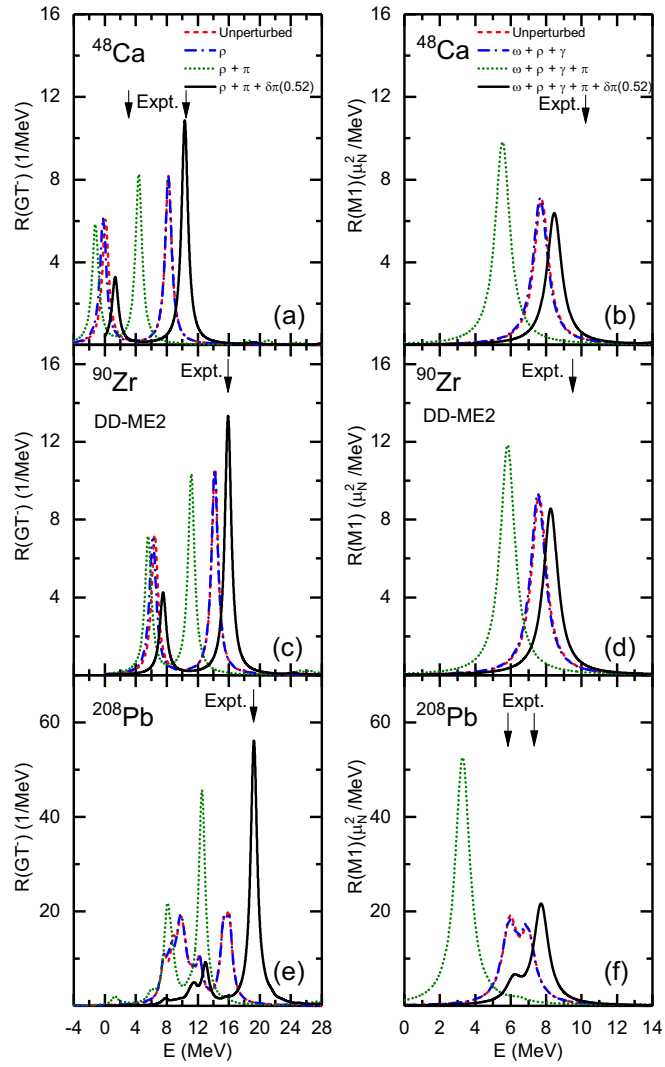

FIG. 1. Response functions of the GT$^-$ (left panel) and $M1$ (right panel) excitations in magic nuclei ^{48}Ca, ^{90}Zr, and ^{208}Pb calculated by the RMF+pnRPA and RMF+RPA approaches, respectively, using the DD-ME2 interaction (solid line), in which the π meson is included and g' is chosen as 0.52. For comparison, the results of unperturbed calculation and those calculations by adding successively the residual interaction from different meson-nucleon couplings on top of it are also shown. A Lorentzian smearing parameter $\Gamma = 1$ MeV is used. The experimental peak energies [85–91] are marked by vertical arrows.

For GT excitations, the unperturbed calculations, in which no residual interactions are included, present two distinct peaks for ^{48}Ca and ^{90}Zr, while the two-peak structure remains in ^{208}Pb but with a broader bump for the low-lying peak. Without any residual interactions, the experimental energies are underestimated by 3–4 MeV. By including the contribution of ρ-N isovector-vector coupling in the residual interaction, the results have almost no changes compared with the unperturbed ones. It is the π-N isovector-pseudovector couplings that make significant changes on the GT transition strength distributions and finally reproduce the experimental data. When the contribution of the π meson is included, both

TABLE I. Theoretical and experimental excitation energies with respect to parent nucleus (shifted by binding energy difference between parent and daughter nucleus) and transition strengths of GT excitations in ^{48}Ca, ^{90}Zr, and ^{208}Pb. The total transition strengths are given in percentages of the Ikeda sum rule value $3(N-Z)$, and the theoretical results are calculated by pnRRPA with DD-ME2 interaction including π meson and pionic counterterm $\delta\pi$ ($g' = 0.52$) in the residual interaction.

Nuclei			E(MeV)	B_{GT^-}	$\sum(B_{\mathrm{GT}^-}$-$B_{\mathrm{GT}^+})$ (%)
^{48}Ca	Expt.	[85]	3.1	–	–
			∼10.8	–	–
			0–30	15.3 ± 2.2	43–61
		[86]	3.1		
			∼10.5 (5.0–15.0)		
			0–17.3	–	43
			0–17.3	–	∼70 (after correction)
	DD-ME2		1.34	5.09	–
			10.32	17.04	–
			0–30	26.98	93.2
^{90}Zr	Expt.	[87]	15.9	–	–
			0–57	28.0±1.6	93±5
	DD-ME2		15.91	20.86	–
			0–50	36.88	92.2
^{208}Pb	Expt.	[88]	19.2	–	–
			0–50	–	∼68 ($\sum B_{\mathrm{GT}^-}$)
	DD-ME2		19.24	87.66	–
			0–50	144.88	91.8

of the high- and low-energy peaks of three nuclei are shifted downwards, and thus the positions of the main peaks are even further away from the experimental results. However, the counterterm must be introduced to cancel the hard core arising from the one-pion exchange [92]. After the counterterm of the π meson is also included, with its strength being adjusted to 0.52, the energies of experimental main peaks can be reproduced very well for all three nuclei considered here. It is interesting to notice that for ^{48}Ca, the low-lying GT peak locates at 0.096 MeV, which is obtained by the single-particle transition from $\nu 1f_{7/2}$ to $\pi 1f_{7/2}$. However, with the inclusion of ρ and π mesons, this excitation energy becomes negative due to the attractive nature of their residual interaction. So the further inclusion of pionic contact term is crucial for obtaining physical results.

For $M1$ excitations, the unperturbed results present only one peak for ^{48}Ca and ^{90}Zr, which is from the spin-flip transition of $j_> \to j_<$. Compared to the GT excitations, the core-polarization transition of $j_> \to j_>$ or $j_< \to j_<$, which leads to the lower peak in GT, is no longer possible. For ^{208}Pb, the unperturbed results still present two peaks comparable in strength as the GT case, since there are two possible spin-flip transitions in ^{208}Pb. Similarly as in the GT case, the inclusion of ω-N isoscalar-vector coupling, ρ-N isovector-vector coupling, and photon field in the residual interaction contribute almost nothing to the $M1$ transition strength distributions. If the contribution of π meson is included, then the excitation energies are shifted downwards to the low-energy region and further diverge from the experimental data, which shows the residual interaction arising from π-N pseudovector coupling is attractive for $M1$, which is the same role as in GT excitations. For ^{208}Pb, the two-peak structure disappears and only one peak is merged with the inclusion of π meson. As presented in the discussion of GT resonance, the pionic zero-range counterterm $\delta\pi$ provides appreciable repulsive contributions to the RPA residual interaction, which are crucial to reproduce the experiment data. One may naturally expect the inclusion of the pionic counterterm can improve the description of $M1$ as well. Taking this counterterm into account with $g' = 0.52$, which was determined by reproducing energies of GT resonance in selected nuclei, we find that the peak energies of $M1$ transitions in all these three nuclei become significantly higher. In particular, the strength distribution of ^{208}Pb becomes fragmented again, and both peak energies get quite close to the experimental data. Even though the peak energies of ^{48}Ca and ^{90}Zr are still lower than the corresponding data, the difference between the theoretical and experimental results are less than 2 MeV and 1 MeV, respectively.

For the convenience of quantitative analysis, the calculated peak energies, as well as the corresponding transition strengths of the GT and $M1$ excitations are displayed in Tables I and Table II, respectively. Available experimental values are also presented for comparison. For GT states, the excitation energies are given with respect to the parent nucleus, so the energies obtained from experiment with respect to the daughter nucleus are shifted by the binding energy difference between parent and daughter nucleus. As shown in Table I, the peak energies of GT$^-$ obtained from pnRRPA calculation reproduce the experimental data well for all three nuclei considered here. For ^{48}Ca, ^{90}Zr, and ^{208}Pb, the theoretical transition strength difference of GT$^-$ and GT$^+$ excitations, i.e., $\sum(B_{\mathrm{GT}^-} - B_{\mathrm{GT}^+})$, calculated by DD-ME2 effective interaction with π meson and its counterterm $\delta\pi$ ($g' = 0.52$), exhaust the Ikeda sum rule values $3(N-Z)$ with the percentages 93.2% (in the energy range of 0–30 MeV), 92.2%, and 91.8% (in the energy range of 0–50 MeV), respectively. The experimental strength is much quenched compared to the

TABLE II. Peak energies and transition strengths of $M1$ excitations in ^{48}Ca, ^{90}Zr, and ^{208}Pb with DD-ME2 interaction including π meson and $\delta\pi$ ($g' = 0.52$) in the RRPA residual interaction. The experimental data from Refs. [89–91,93–100] are also shown for comparison.

Nuclei			E_x(MeV)	B_{M1} (μ_{N}^2)
^{48}Ca	Expt.	[93]	10.227	4.0 ± 0.3
		[96]	10.23	3.9 ± 0.3
			7.7–12.7	5.3 ± 0.6
		[99]	10.23	6.8 ± 0.5
		[89]	10.23	3.85(32)–4.63(38)
	DD-ME2		8.46	10.05
^{90}Zr	Expt.	[94]	8.90 ± 0.15	–
		[97]	8.1–10.5	6.7
		[90]	9.53 ± 0.06	–
		[100]	9(centroid)	–
			7–11	4.17(56)
	DD-ME2		8.26	13.29
^{208}Pb	Expt.	[98]	7.3	15.6
			<6.4	$1.9^{+0.7}_{-0.4}$
		[91]	5.85	2.0
			7.1–8.7	17.9
		[89]	6.5–9.0	20.5(13)
	DD-ME2		6.18	7.23
			7.73	32.92

Ikeda sum rule, which is the famous quenching problem. By extending the measurement of transition strength up to high excitation energies like 57 MeV, some strengths are recovered, for example, for ^{90}Zr, 85–95% of Ikeda sum rule was found in experiment. Up to 30 MeV, RPA calculations already give almost the full Ikeda sum rule, and the strengths that RPA calculations overestimate can be shifted to higher energy region with the inclusion of tensor force [101,102], two-particle–two-hole configurations [103] or particle-vibration coupling [104], and the Δ-isobar excitation [105]. For $M1$ excitations, the peak energies cannot be uniformly reproduced with comparable accuracy with the same g', as shown in Table II. In comparison with the experimental data, the discrepancy for ^{208}Pb is about 400 keV, while they are about 1.2 MeV for ^{90}Zr and 1.7 MeV for ^{48}Ca. For the transition strength, the RPA calculations also overestimate the experimental data systematically, just as the GT case.

TABLE IV. Energy-weighted sum rule $\mathrm{m}_1^{\mathrm{RRPA}}$ (in the energy range of 0–200 MeV) for $M1$ transition in ^{48}Ca, ^{90}Zr, and ^{208}Pb with DD-ME2 interaction including π meson and $\delta\pi$ ($g' = 0.52$) obtained with the RRPA method, in comparison with the Kurath sum rule.

Nuclei	m_1^{RRPA}	m_1^{Kurath}	$m_1^{\mathrm{RRPA}}/m_1^{\mathrm{Kurath}}$
^{48}Ca	102.68	106.91	96.05%
^{90}Zr	129.75	134.53	96.45%
^{208}Pb	347.27	361.20	96.14%

To see the contribution of the α-h configurations, we calculate the transition strengths by excluding the α-h configurations in Eq. (15). The transition strengths of the main excitation states of GT and M1 transitions for ^{48}Ca, ^{90}Zr, and ^{208}Pb are shown in Table III, in comparison with the results of the full calculation using both p-h and α-h configurations. It can be seen that the effects of the α-h configurations are in general negligible, since these states are mainly formed by p-h configurations.

To test the validity of the RRPA for $M1$ excitations, the energy-weighted sum rule $\mathrm{m}_1^{\mathrm{RRPA}}$ calculated by RRPA with DD-ME2 is compared with the results of Kurath sum rule $\mathrm{m}_1^{\mathrm{Kurath}}$ calculated by Eq. (27). As presented in Table IV, the theoretical energy-weighted strength of ^{48}Ca, ^{90}Zr, and ^{208}Pb exhaust the Kurath sum rule with percentages 96.05%, 96.45%, and 96.14%, respectively. Such a result indicates that $\mathrm{m}_1^{\mathrm{RRPA}}$ values are well consistent to the Kurath sum rule $\mathrm{m}_1^{\mathrm{Kurath}}$, and thus the validity of the RRPA is sufficiently supported. The still missing part of the sum rule is supposed to be found through the $M1$ strength of the negative-energy excitation states formed mainly by the α-h configurations.

In the above calculations, the parameter g' in pionic counterterm was taken as 0.52 for DD-ME2 interaction, which was determined by best reproducing experimental energy of GT resonance in ^{208}Pb. However, it turns out that this value is not the best for $M1$ excitations. So in Fig. 2, we will study the effect of pionic counterterm with different g' values of 0, 0.52, 0.85, and 1.50 on $M1$ strength distributions in ^{48}Ca, ^{90}Zr, and ^{208}Pb. It is clear that the pionic counterterm is a repulsive residual interaction, and thus the energies of $M1$ are pushed up for all three nuclei. Without the pionic counterterm, i.e., $g' = 0$, the $M1$ excitation energies are largely underestimated. At $g' = 0.52$, the excitation energies for ^{208}Pb are best

TABLE III. Transition strengths of the main GT$^-$ and $M1$ excitation states in ^{48}Ca, ^{90}Zr, and ^{208}Pb calculated without (W/O) α-h configurations in Eq. (15), in comparison with the results of the calculation with (W/I) both the p-h and α-h configurations. The calculations are performed by pnRRPA and RRPA with DD-ME2 interaction including π meson and pionic counterterm $\delta\pi$ ($g' = 0.52$) in the residual interaction.

	GT$^-$			M1[a]		
Nuclei	E_x(MeV)	B_{GT^-}(W/I)	B_{GT^-}(W/O)	E_x(MeV)	B_{M1}(W/I)	B_{M1}(W/O)
^{48}Ca	10.32	17.04	16.99	8.46	10.05	10.03
^{90}Zr	15.91	20.86	20.80	8.26	13.39	13.35
^{208}Pb	19.24	87.66	87.38	7.73	32.92	32.82

[a]The unit μ_{N}^2 is neglected for simplicity.

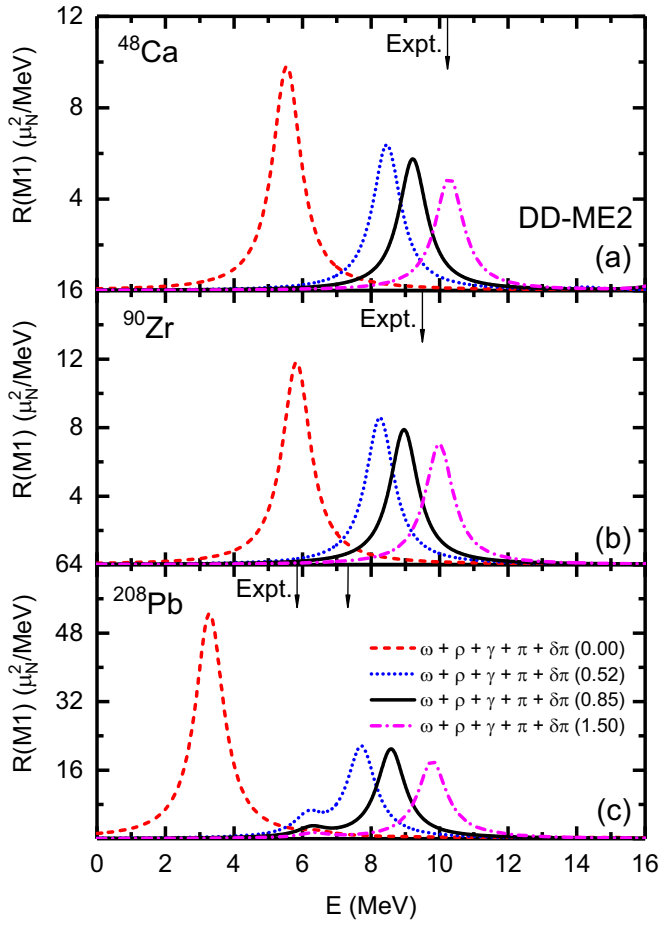

FIG. 2. The $M1$ response function in ^{48}Ca (a), ^{90}Zr (b), and ^{208}Pb (c) calculated with different strength of the zero-range pionic counterterm $\delta\pi$ using DD-ME2 interaction. The calculation excluding pion ($f_\pi = 0$) (dashed line) is also shown for comparison. The experimental peak energies in ^{48}Ca [89], ^{90}Zr [90], and ^{208}Pb [89] are marked by vertical arrows.

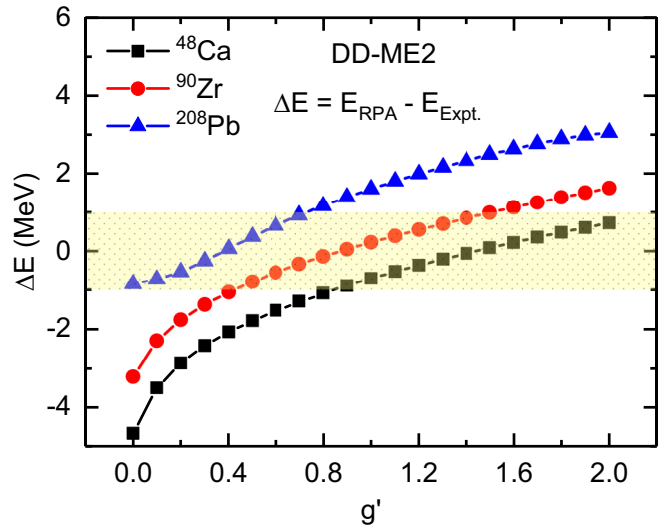

FIG. 3. The difference of peak energies ΔE between theoretical results $E_{\rm RPA}$ and experimental data $E_{\rm Expt.}$ of ^{48}Ca, ^{90}Zr, and ^{208}Pb. Theoretical results are calculated by DD-ME2 with the counterterm parameter g' from 0.0 to 2.0. The light yellow area is the discrepancy lower than 1 MeV.

reproduced; however, the repulsive effect from the counterterm is still insufficient for the $M1$ transitions in ^{48}Ca and ^{90}Zr. At $g' = 0.85$, it gives the minimum root-mean-square deviation ΔE of the calculated peak energies with respect to the corresponding experimental values in these three nuclei, with $\Delta E = 0.98$ MeV. It overestimates the main peak energy of ^{208}Pb by 1.28 MeV, while it still underestimates the peak energy of ^{48}Ca and ^{90}Zr by 0.98 and 0.53 MeV. At $g' = 1.5$, it reproduces best the peak energy of ^{48}Ca; however, the repulsion effect is too strong for ^{90}Zr and ^{208}Pb, which substantially overestimates their excitation energies. Therefore, it is unlikely to simultaneously describe the peak energies of $M1$ transitions in all these three nuclei with the same high accuracy as in the GT cases by only adjusting the parameter g' in the counterterm. This is further confirmed by Fig. 3, where it shows that by increasing the value of g', the shifted energies increase almost linearly with similar slopes, and hence the evolution trends with g' of discrepancies with experimental data are always almost parallel with each other for these three nuclei.

To look for a better description of $M1$ excitations, we also explored different relativistic density functionals, such as DD-ME1 and PKDD. Displayed in Fig. 4 are the $M1$ excitation strength distributions in ^{48}Ca, ^{90}Zr, and ^{208}Pb calculated using DD-ME2, DD-ME1, and PKDD. It is generally found that the pionic counterterm plays the same important role with a repulsive effect and that the g' suggested by the calculation of GT resonance, i.e., $g' = 0.55$ and 0.56 for DD-ME1 and PKDD, respectively, are proper only for ^{208}Pb but too small for ^{48}Ca and ^{90}Zr in describing the peak energies of the $M1$ transition, just being the same case as DD-ME2. Thus, for effective interactions DD-ME1 and PKDD, we also find the optimal value of g' by minimizing the root-mean-square deviation ΔE between theoretical and experimental peak energies of these three nuclei, like what we have done above for DD-ME2. It turns out that the optimal values of g' are 0.97 and 0.75 for DD-ME1 and PKDD, respectively, and their corresponding $\Delta E = 1.00$ and 0.87 MeV, where PKDD gives the best results compared with experimental data. However, in general, the three effective interactions, DD-ME1, DD-ME2, and PKDD, present very similar response functions with the optimal g', as shown in Fig. 4. So the present choices of other relativistic density functionals DD-ME1 and PKDD did not get much improvement on the description of $M1$ excitations compared to DD-ME2.

In order to improve the description of $M1$ excitation for all three nuclei at the same time, we try to include medium effects in the π-meson coupling. For the effective nucleon-nucleon interaction based on the one-boson exchange, the medium effects caused by the many-body correlation could be expressed as the density-dependent coupling strength [92]. The density-dependent form of the π-meson coupling strength in Eq. (17) and Eq. (18) can take the following exponential

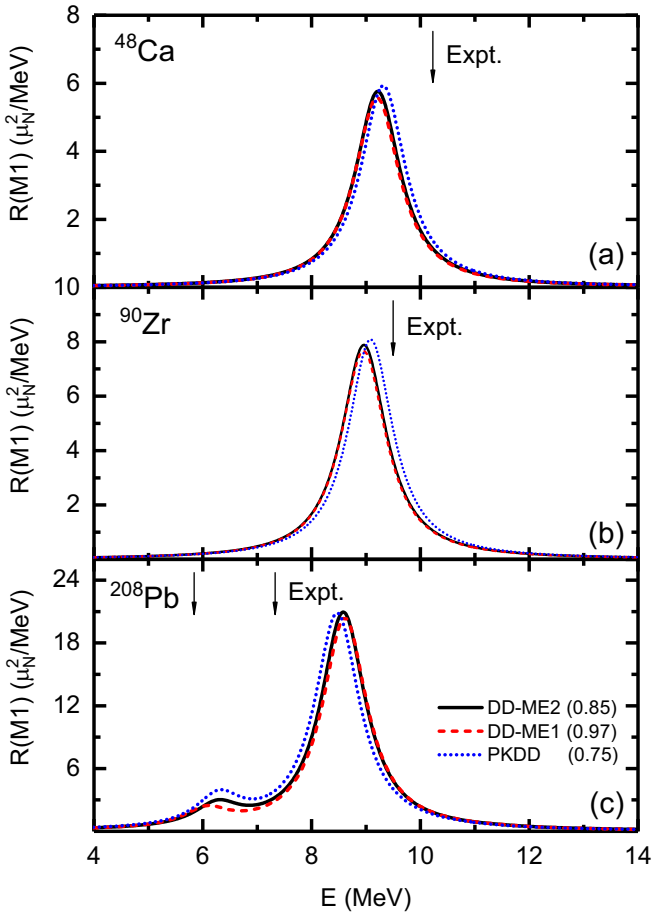

FIG. 4. The $M1$ response function in ^{48}Ca, ^{90}Zr, and ^{208}Pb calculated by RMF+RPA theory with effective interactions DD-ME2 (solid line), DD-ME1 (dashed line), and PKDD (dash-dotted line). The coefficient of counterterm $\delta\pi$, i.e., g', are chosen as the optimal value by minimizing the difference between theoretical and experimental peak energies of these three nuclei, which are 0.85 for DD-ME2, 0.97 for DD-ME1, and 0.75 for PKDD. Their root-mean-square deviations ΔE between theoretical and experimental peak energies of these three nuclei are 0.98 MeV, 1.00 MeV, and 0.87 MeV, respectively. See the text for details.

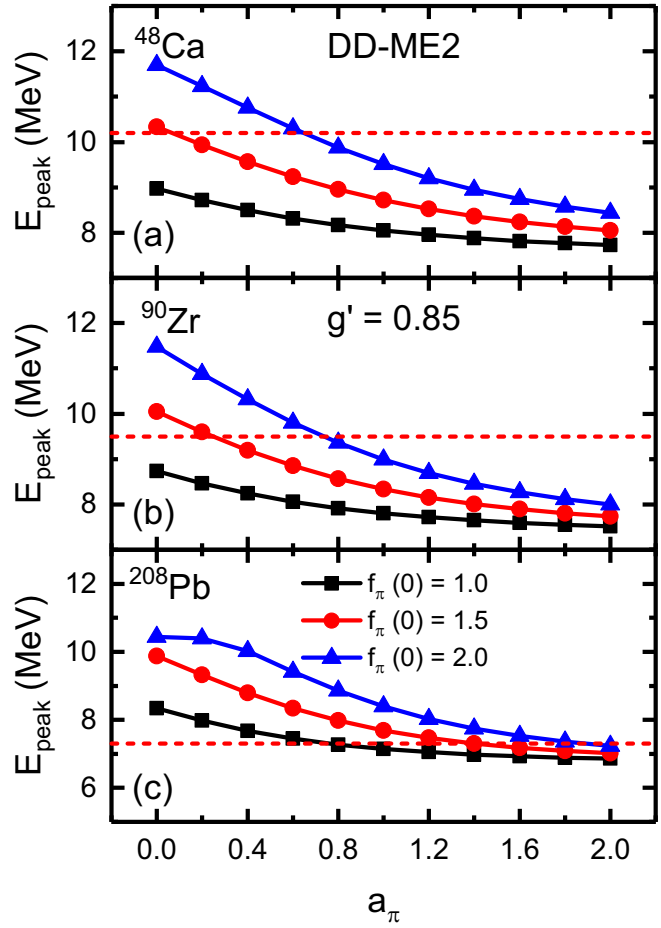

FIG. 5. The evolution of $M1$ excitation peak energy E_{peak} as a function of the coefficient of density dependence a_π for three different zero-density coupling constant $f_\pi(0) = 1.0$ (filled squares), 1.5 (filled circles), and 2.0 (filled triangles) in ^{48}Ca (a), ^{90}Zr (b), and ^{208}Pb (c). The red dashed lines denote experimental peak energies of $M1$ excitation for those three nuclei.

form, as suggested in Refs. [106,107],

$$f_\pi(\rho_b) = f_\pi(0)e^{-a_\pi \frac{\rho_b}{\rho_0}}, \tag{34}$$

where ρ_b denotes the nucleon density, ρ_0 is the saturation nucleon density in symmetric nuclear matter, $f_\pi(0)$ presents the coupling strength at zero density, and a_π is the coefficient of density dependence. When $a_\pi = 0$ and $f_\pi(0) = 1.0$, it reduces to the coupling constant of f_π previously taken in Eq. (19). Adopting this form, we will explore the medium effect of π meson in the residual interaction by changing the coefficient of density dependence a_π with different zero-density coupling strengths $f_\pi(0)$. So in Fig. 5, based on interaction DD-ME2, the peak energies of the $M1$ transitions of ^{48}Ca, ^{90}Zr, and ^{208}Pb are displayed as a function of a_π, with $f_\pi(0) = 1.0$ (filled squares), 1.5 (filled circles), and 2.0 (filled triangles). The parameter g' in the zero-range counterterm is fixed as the optimal value 0.85 determined with constant f_π as shown in Fig. 4.

For a fixed a_π, the peak energy of $M1$ excitation for selected nuclei is higher with larger zero-density constant $f_\pi(0)$. The difference is bigger at small a_π values and becomes smaller with increasing a_π. As mentioned above, π-N coupling gives an attractive contribution, and its counterterm $\delta\pi$ gives a repulsive contribution in the p-h residual interaction. With $g' = 0.85$, the $\delta\pi$ counterterm gives a larger contribution than the π-N coupling does. As a result, the sum of two terms gives a repulsive contribution, and the repulsion becomes stronger with larger $f_\pi(0)$. For a fixed $f_\pi(0)$, the peak energy shifts to lower energy with the increasing of a_π. While a_π is increasing, the coupling strength $f_\pi(\rho_b)$ decreases faster with density and gets a smaller value. As a result, the repulsion becomes weaker at large a_π, and the excitation energy is also decreased.

Compared to experimental data (dashed line) of the $M1$ peak energy, the most suitable parameters are $f_\pi(0) = 2.0$ and $a_\pi = 0.6$ for ^{48}Ca, $f_\pi(0) = 1.5$ and $a_\pi = 0.2$ for ^{90}Zr, as well

TABLE V. The main transition configurations as well as their contributions to the total sum of RRPA amplitudes $\sum_{cd}(X^2_{cd} - Y^2_{cd})$ for the GT and $M1$ excitation states at the peak energies E_x in ^{48}Ca, ^{90}Zr, and ^{208}Pb, which are calculated by DD-ME2 interaction with the same $g' = 0.52$.

	$M1$			GT$^-$		
Nuclei	E_x (MeV)	Configurations	$\sum_{cd} X^2_{cd} - Y^2_{cd}$	E_x (MeV)	Configurations	$\sum_{cd} X^2_{cd} - Y^2_{cd}$
^{48}Ca	8.46	$[\nu 1f_{5/2}, \nu 1f^{-1}_{7/2}]$	99.70%	10.32	$[\pi 1f_{5/2}, \nu 1f^{-1}_{7/2}]$	94.77%
					$[\pi 1f_{7/2}, \nu 1f^{-1}_{7/2}]$	4.29%
^{90}Zr	8.26	$[\nu 1g_{7/2}, \nu 1g^{-1}_{9/2}]$	99.79%	15.91	$[\pi 1g_{7/2}, \nu 1g^{-1}_{9/2}]$	96.28%
					$[\pi 1g_{9/2}, \nu 1g^{-1}_{9/2}]$	3.00%
^{208}Pb	7.73	$[\nu 1i_{11/2}, \nu 1i^{-1}_{13/2}]$	84.51%	19.24	$[\pi 1i_{11/2}, \nu 1i^{-1}_{13/2}]$	47.76%
		$[\pi 1h_{9/2}, \pi 1h^{-1}_{11/2}]$	15.17%		$[\pi 1h_{9/2}, \nu 1h^{-1}_{11/2}]$	29.56%

as $f_\pi(0) = 1.0$ and $a_\pi = 0.8$ for ^{208}Pb, which perfectly reproduce all the experimental data. However, it cannot reproduce the experimental data simultaneously with unified parameters. Although the coefficient of density dependence a_π can take the same value 0.6 or 0.8, the $f_\pi(0)$ still needs to take very different values such as $f_\pi(0) = 2.0$, 2.0, and 1.0 for ^{48}Ca, ^{90}Zr, and ^{208}Pb, respectively, in order to give an overall good description of experimental data. On the other hand, by taking the same $f_\pi(0)$ as 2.0, the a_π needs to take different values of 0.6, 0.8, and 2.0 for ^{48}Ca, ^{90}Zr, and ^{208}Pb, respectively. So the inclusion of density dependence in isovecotor-pseudovector coupling does not solve the problem of a unified description of $M1$ excitations from ^{48}Ca to ^{208}Pb. This forces us to further explore the deep reasons why the inclusion of π-N coupling could unifiedly describe very well the GT excitations from ^{48}Ca to ^{208}Pb but fails in the $M1$ excitations.

In order to understand the problem, in Table V, the dominant p-h excitation configurations and the contribution of each configuration evaluated by $(X^2_{cd} - Y^2_{cd})$, where $\sum_{cd}(X^2_{cd} - Y^2_{cd})$ is normalized to one, for GT and $M1$ excitation states at the peak energies in ^{48}Ca, ^{90}Zr, and ^{208}Pb are listed. From the dominant configurations, it is also clear to see that the spin-flip $M1$ excitation is the analog state of GT resonance, where the difference in their dominant configurations only reflects in isospin space, except a small component of core-polarization transition in GT state for ^{48}Ca and ^{90}Zr which is absent in $M1$ state. The dominant configurations involve spin-orbit partner states near the Fermi surface for all three nuclei.

Taking ^{48}Ca and ^{208}Pb as examples, we show in Fig. 6 the dominant p-h transition configurations calculated with the effective interaction DD-ME2, and for comparison, the related experimental single-particle levels are also shown. For ^{208}Pb, due to the limited experimental data, only the main configuration of $[1i_{11/2}, 1i^{-1}_{13/2}]$ is shown. For GT state in ^{48}Ca, the main p-h configuration is $[\pi 1f_{5/2}, \nu 1f^{-1}_{7/2}]$. The calculated unperturbed energy is 8.22 MeV while the experimental datum is 5.40 MeV. For the GT state in ^{208}Pb, the main p-h configuration is $[\pi 1i_{11/2}, \nu 1i^{-1}_{13/2}]$. The calculated unperturbed energy is 16.07 MeV, while the experimental datum is 12.65 MeV. The calculations overestimate the experimental values by about 3 MeV in both cases. Although the unperturbed energies do not agree well with experimental data, the GT energy can be well reproduced by the inclusion of residual interaction. Since for both nuclei the unperturbed energies are overestimated by a similar value, by taking the same g' value in the pionic counterterm, the GT resonance energy of ^{48}Ca and ^{208}Pb can be simultaneously reproduced. However, for $M1$ excitations, the cases are different. The unperturbed energy is just the spin-orbit splitting of the f orbital for

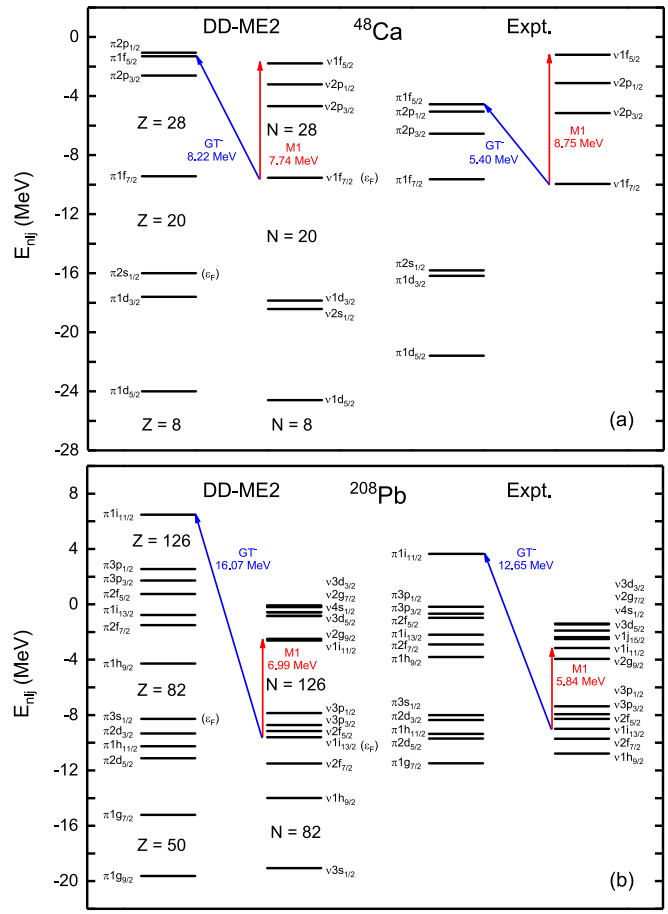

FIG. 6. Proton and neutron single-particle spectra in ^{48}Ca (a) and ^{208}Pb (b) obtained from RMF calculation with Lagrangian DD-ME2. Dominating transition configurations of GT$^-$ and $M1$ excitation for ^{48}Ca and ^{208}Pb are indicated by red and blue arrows. Experimental single-particle spectra from Ref. [108] are also presented for comparison.

^{48}Ca and the i orbital for ^{208}Pb. The spin-orbit splitting of the f orbital calculated within RMF by DD-ME2 interaction underestimates the experimental value by 1 MeV, while that of the i orbital overestimates the experimental value by 1 MeV. As a result, ^{48}Ca needs a larger repulsive residual interaction, which is reflected in a larger g' value, to reproduce the experimental $M1$ energy, compared to what ^{208}Pb needs. So it is difficult to reproduce the experimental data for ^{48}Ca and ^{208}Pb simultaneously with the same g' value. This indicates that new relativistic effective interactions aiming at proper spin-orbit splitting are appealing to improve the description of the $M1$ resonance.

IV. SUMMARY

In this work, magnetic dipole ($M1$) resonances of magical nuclei ^{48}Ca, ^{90}Zr, and ^{208}Pb have been studied within the random-phase approximation based on the relativistic mean-field theory, using the density-dependent effective interactions. The contribution of the π meson, including that of the zero-range counterterm, is considered in the residual interaction. Based on the RMF theory, the Kurath sum rule which consists of the isovector, isoscalar, and their interference components has been derived. The validity of our calculation has been certified by producing the Kurath sum rule. By analyzing the contribution of each meson-nucleon coupling, we conclude that the π meson plays a very important role in determining the energy distribution of the $M1$ resonances. Meanwhile, it is found that the strength of the counterterm suggested to reproduce the Gamow-Teller resonances properly reproduces the peak energies of $M1$ in ^{208}Pb but underestimates the peak energies of ^{48}Ca and ^{90}Zr. By properly enlarging the strength of the zero-range counterterm of the π meson, it can shift the peak energies of ^{48}Ca and ^{90}Zr closer to the experimental value, but the peak energy of ^{208}Pb is pushed further away. Such a conclusion generally holds for currently existing density-dependent meson-exchange interactions like DD-ME1, DD-ME2 and PKDD, even with an inclusion of the density-dependent coupling constant in π-meson coupling. To explore the underlying reason, we studied the relevant single-particle structure of main p-h configurations for GT state and $M1$ state. It is found that the spin-orbit splitting of the f orbital relevant for $M1$ excitation in ^{48}Ca underestimates the experimental data while that of the i orbital in ^{208}Pb overestimates the experimental data, leading to the unified description of $M1$ excitation in ^{48}Ca and ^{208}Pb being impossible. Therefore, suitable spin-orbit splitting is the key to simultaneously reproduce the $M1$ peak energies from light to heavy nuclei. Work on improving spin-orbit splitting with a new effective interaction is now in progress.

ACKNOWLEDGMENTS

This work is partly supported by the National Natural Science Foundation of China under Grants No. 12075104 and No. 11905088; Fundamental Research Funds for the central universities under Grants No. lzujbky-2021-sp41, No. lzujbky-2019-11, and No. lzujbky-2021-sp36; and the Strategic Priority Research Program of Chinese Academy of Sciences under Grant No. XDB34000000.

[1] L. W. Fagg, Rev. Mod. Phys. **47**, 683 (1975).
[2] F. Osterfeld, Rev. Mod. Phys. **64**, 491 (1992).
[3] K. Heyde, P. von Neumann-Cosel, and A. Richter, Rev. Mod. Phys. **82**, 2365 (2010).
[4] K. Langanke, G. Martínez-Pinedo, P. von Neumann-Cosel, and A. Richter, Phys. Rev. Lett. **93**, 202501 (2004).
[5] K. Langanke, G. Martínez-Pinedo, B. Müller, H.-T. Janka, A. Marek, W. R. Hix, A. Juodagalvis, and J. M. Sampaio, Phys. Rev. Lett. **100**, 011101 (2008).
[6] W. Almosly, B. G. Carlsson, J. Suhonen, and E. Ydrefors, Phys. Rev. C **99**, 055801 (2019).
[7] C. Giusti and M. V. Ivanov, J. Phys. G: Nucl. Part. Phys. **47**, 024001 (2020).
[8] H. Loens, K. Langanke, G. Martínez-Pinedo, and K. Sieja, Eur. Phys. J. A **48**, 34 (2012).
[9] S. Goriely, S. Hilaire, S. Péru, M. Martini, I. Deloncle, and F. Lechaftois, Phys. Rev. C **94**, 044306 (2016).
[10] M. R. Mumpower, T. Kawano, J. L. Ullmann, M. Krtička, and T. M. Sprouse, Phys. Rev. C **96**, 024612 (2017).
[11] P. V. Neumann-Cosel and A. Tamii, Eur. Phys. J. A **55**, 110 (2019).
[12] N. L. Iudice and A. Richter, Phys. Lett. B **304**, 193 (1993).
[13] J. Enders, H. Kaiser, P. von Neumann-Cosel, C. Rangacharyulu, and A. Richter, Phys. Rev. C **59**, R1851 (1999).
[14] A. Richter, Prog. Part. Nucl. Phys. **34**, 261 (1995).
[15] N. Pietralla, P. von Brentano, and A. Lisetskiy, Prog. Part. Nucl. Phys. **60**, 225 (2008).
[16] Y. Fujita, B. Rubio, and W. Gelletly, Prog. Part. Nucl. Phys. **66**, 549 (2011).
[17] J. Enders, P. von Neumann-Cosel, C. Rangacharyulu, and A. Richter, Phys. Rev. C **71**, 014306 (2005).
[18] M. Arnould, S. Goriely, and K. Takahashi, Phys. Rep. **450**, 97 (2007).
[19] R. Reifarth, C. Lederer, and F. Käppeler, J. Phys. G: Nucl. Part. Phys. **41**, 053101 (2014).
[20] R. Schwengner, S. Frauendorf, and B. A. Brown, Phys. Rev. Lett. **118**, 092502 (2017).
[21] R. Schwengner and G. Rusev, Phys. Rev. C **100**, 054320 (2019).
[22] K. Sieja, Phys. Rev. C **98**, 064312 (2018).
[23] P. Sarriguren, E. Moya de Guerra, and R. Nojarov, Phys. Rev. C **54**, 690 (1996).
[24] R. Hilton, W. Höhenberger, and P. Ring, Eur. Phys. J. A **1**, 257 (1998).
[25] P. Vesely, J. Kvasil, V. O. Nesterenko, W. Kleinig, P. G. Reinhard, and V. Y. Ponomarev, Phys. Rev. C **80**, 031302(R) (2009).
[26] P. Wen, L.-G. Cao, J. Margueron, and H. Sagawa, Phys. Rev. C **89**, 044311 (2014).
[27] V. Tselyaev, N. Lyutorovich, J. Speth, P.-G. Reinhard, and D. Smirnov, Phys. Rev. C **99**, 064329 (2019).

[28] J. Speth, P.-G. Reinhard, V. Tselyaev, and N. Lyutorovich, Phys. Rev. C **102**, 054332 (2020).
[29] V. O. Nesterenko, J. Kvasil, P. Vesely, W. Kleinig, P.-G. Reinhard, and V. Y. Ponomarev, J. Phys. G **37**, 064034 (2010).
[30] V. Tselyaev, N. Lyutorovich, J. Speth, and P.-G. Reinhard, Phys. Rev. C **102**, 064319 (2020).
[31] L.-G. Cao, G. Colò, H. Sagawa, P. F. Bortignon, and L. Sciacchitano, Phys. Rev. C **80**, 064304 (2009).
[32] L.-G. Cao, H. Sagawa, and G. Colò, Phys. Rev. C **83**, 034324 (2011).
[33] G. Co', V. De Donno, M. Anguiano, and A. M. Lallena, Phys. Rev. C **85**, 034323 (2012).
[34] J. D. Walecka, Ann. Phys. **83**, 491 (1974).
[35] P. G. Reinhard, Rep. Prog. Phys. **52**, 439 (1989).
[36] P. Ring, Prog. Part. Nucl. Phys. **37**, 193 (1996).
[37] M. Bender, P. H. Heenen, and P. G. Reinhard, Rev. Mod. Phys. **75**, 121 (2003).
[38] D. Vretenar, A. V. Afanasjev, G. A. Lalazissis, and P. Ring, Phys. Rep. **409**, 101 (2005).
[39] J. Meng, H. Toki, S. G. Zhou, S. Q. Zhang, W. H. Long, and L. S. Geng, Prog. Part. Nucl. Phys. **57**, 470 (2006).
[40] J. Meng, *Relativistic Density Functional for Nuclear Structure* (World Scientific, Singapore, 2016).
[41] P. W. Zhao, Z. P. Li, J. M. Yao, and J. Meng, Phys. Rev. C **82**, 054319 (2010).
[42] V. Prassa, T. Nikšić, G. A. Lalazissis, and D. Vretenar, Phys. Rev. C **86**, 024317 (2012).
[43] S. Quan, Q. Chen, Z. P. Li, T. Nikšić, and D. Vretenar, Phys. Rev. C **95**, 054321 (2017).
[44] X. W. Xia, Y. Lim, P. W. Zhao, H. Z. Liang, X. Y. Qu, Y. Chen, H. Liu, L. F. Zhang, S. Q. Zhang, Y. Kim *et al.*, At. Data Nucl. Data Tables **121-122**, 1 (2018).
[45] Y. Cao, S. E. Agbemava, A. V. Afanasjev, W. Nazarewicz, and E. Olsen, Phys. Rev. C **102**, 024311 (2020).
[46] A. Taninah, S. E. Agbemava, and A. V. Afanasjev, Phys. Rev. C **102**, 054330 (2020).
[47] U. C. Perera, A. V. Afanasjev, and P. Ring, Phys. Rev. C **104**, 064313 (2021).
[48] K. Q. Lu, Z. X. Li, Z. P. Li, J. M. Yao, and J. Meng, Phys. Rev. C **91**, 027304 (2015).
[49] Y. L. Yang, Y. K. Wang, P. W. Zhao, and Z. P. Li, Phys. Rev. C **104**, 054312 (2021).
[50] G. Accorto, T. Naito, H. Liang, T. Nikšić, and D. Vretenar, Phys. Rev. C **103**, 044304 (2021).
[51] J. N. Ginocchio, Phys. Rev. Lett. **78**, 436 (1997).
[52] H. Z. Liang, J. Meng, and S. G. Zhou, Phys. Rep. **570**, 1 (2015).
[53] P. Zhao, S. Zhang, J. Peng, H. Liang, P. Ring, and J. Meng, Phys. Lett. B **699**, 181 (2011).
[54] P. W. Zhao, J. Peng, H. Z. Liang, P. Ring, and J. Meng, Phys. Rev. Lett. **107**, 122501 (2011).
[55] S. Frauendorf and Jie Meng, Nucl. Phys. A **617**, 131 (1997).
[56] J. Meng, J. Peng, S. Q. Zhang, and S.-G. Zhou, Phys. Rev. C **73**, 037303 (2006).
[57] P. Zhao, Phys. Lett. B **773**, 1 (2017).
[58] C. De Conti, A. Galeão, and F. Krmpotić, Phys. Lett. B **444**, 14 (1998).
[59] C. De Conti, A. Galeão, and F. Krmpotić, Phys. Lett. B **494**, 46 (2000).
[60] Z. Y. Ma, N. Van Giai, A. Wandelt, D. Vretenar, and P. Ring, Nucl. Phys. A **686**, 173 (2001).
[61] H. Z. Liang, N. Van Giai, and J. Meng, Phys. Rev. Lett. **101**, 122502 (2008).
[62] Y. F. Niu, N. Paar, D. Vretenar, and J. Meng, Phys. Rev. C **83**, 045807 (2011).
[63] N. Paar, T. Nikšić, D. Vretenar, and P. Ring, Phys. Rev. C **69**, 054303 (2004).
[64] Z. M. Niu, Y. F. Niu, H. Z. Liang, W. H. Long, and J. Meng, Phys. Rev. C **95**, 044301 (2017).
[65] D. Vale, Y. F. Niu, and N. Paar, Phys. Rev. C **103**, 064307 (2021).
[66] T. Nikšić, D. Vretenar, and P. Ring, Phys. Rev. C **66**, 064302 (2002).
[67] N. Paar, P. Ring, T. Nikšić, and D. Vretenar, Phys. Rev. C **67**, 034312 (2003).
[68] T. Oishi, G. Kružić, and N. Paar, J. Phys. G **47**, 115106 (2020).
[69] T. Oishi, G. Kružić, and N. Paar, J. Phys.: Conf. Ser. **1643**, 012153 (2020).
[70] G. Kružić, T. Oishi, D. Vale, and N. Paar, Phys. Rev. C **102**, 044315 (2020).
[71] G. Kružić, T. Oishi, and N. Paar, Phys. Rev. C **103**, 054306 (2021).
[72] T. Oishi, G. Kružić, and N. Paar, Eur. Phys. J. A **57**, 180 (2021).
[73] H. Yukawa, Proc. Phys. Math. Soc. Jpn. **17**, 48 (1935).
[74] R. Machleidt, Adv. Nucl. Phys. **19**, 189 (1989).
[75] T. Nikšić, D. Vretenar, and P. Ring, Prog. Part. Nucl. Phys. **66**, 519 (2011).
[76] S. Typel and H. Wolter, Nucl. Phys. A **656**, 331 (1999).
[77] G. A. Lalazissis, T. Nikšić, D. Vretenar, and P. Ring, Phys. Rev. C **71**, 024312 (2005).
[78] C. J. Horowitz and J. Piekarewicz, Phys. Rev. C **50**, 2540 (1994).
[79] Z. Y. Ma, B. Q. Chen, N. V. Giai, and T. Suzuki, Eur. Phys. J. A **20**, 429 (2004).
[80] T. Nikšić, D. Vretenar, P. Finelli, and P. Ring, Phys. Rev. C **66**, 024306 (2002).
[81] W. Long, J. Meng, N. Van Giai, and S.-G. Zhou, Phys. Rev. C **69**, 034319 (2004).
[82] P. Ring and P. Schuck, *The Nuclear Many-body Problem* (Springer, New York, 1980).
[83] D. Kurath, Phys. Rev. **130**, 1525 (1963).
[84] M. Traini, Phys. Rev. Lett. **41**, 1535 (1978).
[85] K. Yako, M. Sasano, K. Miki, H. Sakai, M. Dozono, D. Frekers, M. B. Greenfield, K. Hatanaka, E. Ihara, M. Kato, T. Kawabata, H. Kuboki, Y. Maeda, H. Matsubara, K. Muto, S. Noji, H. Okamura, T. H. Okabe, S. Sakaguchi, Y. Sakemi *et al.*, Phys. Rev. Lett. **103**, 012503 (2009).
[86] B. D. Anderson, T. Chittrakarn, A. R. Baldwin, C. Lebo, R. Madey, P. C. Tandy, J. W. Watson, B. A. Brown, and C. C. Foster, Phys. Rev. C **31**, 1161 (1985).
[87] T. Wakasa, H. Sakai, H. Okamura, H. Otsu, S. Fujita, S. Ishida, N. Sakamoto, T. Uesaka, Y. Satou, M. B. Greenfield, and K. Hatanaka, Phys. Rev. C **55**, 2909 (1997).
[88] T. Wakasa, M. Okamoto, M. Dozono, K. Hatanaka, M. Ichimura, S. Kuroita, Y. Maeda, H. Miyasako, T. Noro, T. Saito, Y. Sakemi, T. Yabe, and K. Yako, Phys. Rev. C **85**, 064606 (2012).
[89] J. Birkhan, H. Matsubara, P. von Neumann-Cosel, N. Pietralla, V. Y. Ponomarev, A. Richter, A. Tamii, and J. Wambach, Phys. Rev. C **93**, 041302(R) (2016).

[90] C. Iwamoto, H. Utsunomiya, A. Tamii, H. Akimune, H. Nakada, T. Shima, T. Yamagata, T. Kawabata, Y. Fujita, H. Matsubara, Y. Shimbara, M. Nagashima, T. Suzuki, H. Fujita, M. Sakuda, T. Mori, T. Izumi, A. Okamoto, T. Kondo, B. Bilgier *et al.*, Phys. Rev. Lett. **108**, 262501 (2012).

[91] T. Shizuma, T. Hayakawa, H. Ohgaki, H. Toyokawa, T. Komatsubara, N. Kikuzawa, A. Tamii, and H. Nakada, Phys. Rev. C **78**, 061303(R) (2008).

[92] B. D. Serot and J. D. Walecka, in *Advances in Nuclear Physics*, Vol. 16, edited by J. W. Negele and E. Vogt (Plenum Press, New York, 1986).

[93] W. Steffen, H.-D. Gräf, W. Gross, D. Meuer, A. Richter, E. Spamer, O. Titze, and W. Knüpfer, Phys. Lett. B **95**, 23 (1980).

[94] N. Anantaraman, G. M. Crawley, A. Galonsky, C. Djalali, N. Marty, M. Morlet, A. Willis, and J. C. Jourdain, Phys. Rev. Lett. **46**, 1318 (1981).

[95] R. Köhler, J. A. Wartena, H. Weigmann, L. Mewissen, F. Poortmans, J. P. Theobald, and S. Raman, Phys. Rev. C **35**, 1646 (1987).

[96] W. Steffen, H.-D. Gräf, A. Richter, A. Härting, W. Weise, U. Deutschmann, G. Lahm, and R. Neuhausen, Nucl. Phys. A **404**, 413 (1983).

[97] R. M. Laszewski, R. Alarcon, and S. D. Hoblit, Phys. Rev. Lett. **59**, 431 (1987).

[98] R. M. Laszewski, R. Alarcon, D. S. Dale, and S. D. Hoblit, Phys. Rev. Lett. **61**, 1710 (1988).

[99] J. R. Tompkins, C. W. Arnold, H. J. Karwowski, G. C. Rich, L. G. Sobotka, and C. R. Howell, Phys. Rev. C **84**, 044331 (2011).

[100] G. Rusev, N. Tsoneva, F. Dönau, S. Frauendorf, R. Schwengner, A. P. Tonchev, A. S. Adekola, S. L. Hammond, J. H. Kelley, E. Kwan, H. Lenske, W. Tornow, and A. Wagner, Phys. Rev. Lett. **110**, 022503 (2013).

[101] C. L. Bai, H. Sagawa, H. Q. Zhang, X. Z. Zhang, G. Colò, and F. R. Xu, Phys. Lett. B **675**, 28 (2009).

[102] C. L. Bai, H. Q. Zhang, X. Z. Zhang, F. R. Xu, H. Sagawa, and G. Colò, Phys. Rev. C **79**, 041301(R) (2009).

[103] G. F. Bertsch and I. Hamamoto, Phys. Rev. C **26**, 1323 (1982).

[104] Y. F. Niu, G. Colò, and E. Vigezzi, Phys. Rev. C **90**, 054328 (2014).

[105] B. Brown and B. Wildenthal, Nucl. Phys. A **474**, 290 (1987).

[106] W. H. Long, N. Van Giai, and J. Meng, Phys. Lett. B **640**, 150 (2006).

[107] W. H. Long, H. Sagawa, J. Meng, and N. Van Giai, Europhys. Lett. **82**, 12001 (2008).

[108] H. Grawe, K. Langanke, and G. Martínez-Pinedo, Rep. Prog. Phys. **70**, 1525 (2007).